Event-Triggering Virtual Inertia Control of PV Systems with Power Reserve

Peng, Qiao; Tang, Zhongting; Yang, Yongheng; Liu, Tianqi; Blaabjerg, Frede

Published in:
IEEE Transactions on Industry Applications

DOI (link to publication from Publisher):
10.1109/TIA.2021.3080227

Publication date:
2021

Document Version
Accepted author manuscript, peer reviewed version

Event-Triggering Virtual Inertia Control of PV Systems with Power Reserve

Qiao Peng, *Member, IEEE,* Zhongting Tang, *Member, IEEE,* Yongheng Yang, *Senior Member, IEEE,* Tianqi Liu, *Senior Member, IEEE,* and Frede Blaabjerg, *Fellow, IEEE*

***Abstract*—Grid frequency support, e.g., by the virtual inertia control (VIC), of photovoltaic (PV) systems, is more demanded than ever before. To achieve the full-range frequency support (i.e., to tackle the under- or over-frequency issues), the power reserve is necessary for PV systems. Accordingly, a power reserve control (PRC) method based on the maximum power point tracking (MPPT) is adopted in this paper, referring to as MPPT-PRC. It measures the real-time maximum available power (MAP) periodically, being independent of physical sensors and burdensome computation. However, the MAP measurement loop inevitably couples with the power reserve loop, which makes the realization of the VIC challenging. Aiming at this issue, an event-triggering strategy is elaborately designed to switch the PV system in-between different operating modes. The strategy is realized by a set of control signals. They are responsible for the detection of frequency incidents, the activation of MPPT, the measurement of MAP, respectively. Consequently, the VIC can be achieved based on the MPPT-PRC without any conflicts or instability. Experimental tests are performed on StarSim real-time hardware-in-the-loop (RT-HIL) system to validate the proposed MPPT-PRC-based VIC, as well as the coordination of the control loops.**

***Index Terms*—Photovoltaic (PV) system; virtual inertia control (VIC); frequency regulation; maximum power point tracking (MPPT); power reserve; event-triggering**

I. Introduction

THE penetration of renewable energy sources (RESs) in the modern power system is still increasing with a fast growth rate. The photovoltaic (PV) system contributes considerably to the national and global energy transition, and it is still developing [1], [2]. In such a case, the PV systems should support the grid more frequently rather than being solely power generating units, where one of the emerging demands from the grid is the frequency response. On one hand, the RESs should perceive the sudden power generation loss of the grid and ride through it to avoid further cascading failures, e.g., frequency collapses, like what has happened in Australia [3] and the UK [4]. On the other hand, the ancillary frequency regulation of RESs is being required by the industry, including the frequency droop control and the inertia response [5]–[7]. The latter is becoming more important than ever before, as the power grid is continuously being hybridized with more RESs.

In the modern power system, the conventional synchronous generators (SG) are being replaced by distributed RESs. Consequently, the mechanical inertia generated by the SG rotors is decreasing. It makes the modern power grid inertialess or low inertia-based [8]. The mechanical inertia governs the balance between the active power generation and demand, based on which the frequency is maintained [9]. Thus, the decrease of mechanical inertia challenges the grid frequency stability and alternative inertia is demanded. Various inertia emulation strategies of power converters were proposed to enhance the system inertia [10], [11], which inspires the exploration of the inertia provision of RESs.

Due to the large capacity and flexible output regulation, the PV system can be a promising solution to the inertia provision [12]. For instance, the synchronous power controller for PV power plants was proposed in [13], [14] to provide virtual inertia, which can also be attained by small-scale grid-connected single-phase rooftop PV systems [15]. In addition, the inertia can be generated during the charging/discharging of the DC-link capacitors in PV systems [16]. Nevertheless, in these strategies, the energy for inertia emulation comes mainly from the energy storage units, e.g., DC-link capacitors or batteries, instead of managing the generation from the PV panels. It means extra hardware investments are inevitable; otherwise, the amount of the emulated inertia is very limited.

Alternatively, independent of the energy storage units, a power reserve control (PRC) can be implemented in PV systems, enabling flexible frequency regulation [17], where the power reserve operation replaces the energy storage units to be "an energy buffer". Conventionally, the PV system operates at the maximum power point (MPP) to deliver the maximum available power (MAP) to the grid. When the frequency regulation is required by the grid, this operation should be altered accordingly. For instance, when the load demand is more than the generation, the frequency will decrease, referring to as under-frequency issues, and more power is required from the PV systems to balance the demand and generation. To do so, PV systems should firstly operate with power curtailment at one of the power reserve points (PRP), as shown in Fig. 1. Then, extra power can be provided by PV systems. This is referred to as PRC-based frequency regulation.

Various PRC methods are adopted in the literature, where the measurement of the MAP is a challenging issue. The master-slave method achieves the MAP measurement by master PV unit(s), and then, the slave units are controlled with power reserve [18]–[20]. Although it is simple, communication is required. Moreover, master PV unit(s) should be

This work was supported by THE VELUX FOUNDATIONS under the VILLUM Investigator Grant – REPEPS (Award Ref. No.: 00016591). The paper was virtually presented in part at IEEE APEC 2020, 15-19 March 2020. *(Corresponding author: Yongheng Yang.)*

Q. Peng and T. Liu are with the College of Electrical Engineering, Sichuan University, Chengdu 610065, China (e-mail: qpeng@scu.edu.cn; tqliu@scu.edu.cn).

Z. Tang and F. Blaabjerg are with the Department of Energy Technology, Aalborg University, Aalborg 9220, Denmark (e-mail: zta@et.aau.dk; fbl@et.aau.dk).

Y. Yang is with the College of Electrical Engineering, Zhejiang University, Hangzhou 310027, China (e-mail: yang_yh@zju.edu.cn).

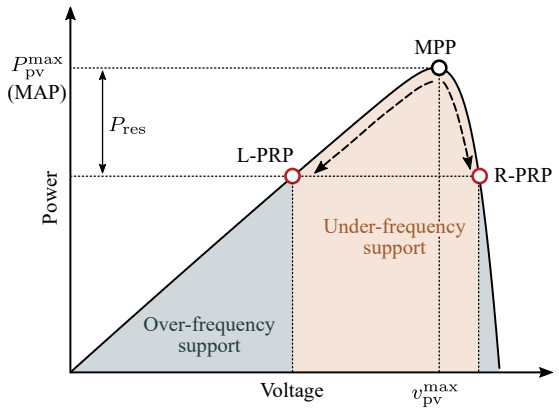

Fig. 1. Power reserve demands to a PV system for frequency control, where, $P_{\rm pv}^{\rm max}$ and $P_{\rm res}$ are the maximum PV power and the required power reserve, $v_{\rm pv}^{\rm max}$ is the PV voltage corresponding to $P_{\rm pv}^{\rm max}$ (MAP – maximum available power, MPP – maximum power point, L-PRP – left power reserve point, R-PRP – right power reserve point).

carefully selected or a backup solution is required to ensure the estimation accuracy [21]. Alternatively, according to the irradiance and temperature data collected by sensors, the real-time MAP can be estimated, and the PRP can be calculated [16], [22]–[24]. However, the wide application of this method is limited by the high cost of sensors. Curve-fitting methods are also attractive [25], [26]. The MAP is estimated based on the sampled PV voltage and current, of which the accuracy highly depends on the curve-fitting algorithms and the selected samples [27]. Although this method does not require any hardware modification, it introduces heavy computational burden, and the estimation error may increase with the aging of the PV panels. In addition, the MAP can be estimated by empirical models, e.g., the short-circuit PV current estimation function and the Lambert-W function, with several sampling points [28], [29]. However, the accuracy of the empirical model may not be maintained with the components aging. Moreover, many approximations are made, leading to inevitable errors.

In all, the prior-art methods either require additional hardware or heavy computation, which is non-economical or computationally intensive. For this, a more application-friendly sensorless PRC method was proposed in [30]. It is developed from the general perturb and observe (P&O)-MPPT algorithm. It perturbs the PV system operating point to the MPP periodically, and then, the operating point is perturbed to the PRP. This method is independent of communication, sensors, or curve-fitting algorithms. It is not limited to PV converter topologies or system configurations either. However, in this method, the P&O strategy is applied to make the PV system operate at the PRP. It limits the realization of frequency regulation to a large extent, especially inertia emulation. The reason is that the incremental PV power for frequency support in each perturbation step is difficult to calculate. To tackle this issue, an improved method was presented in [31], where a proportional-integral (PI) controller is adopted in the power reserve mode to reach the PRP. It makes the PV power regulation more flexible, while it also couples with the basic control of the PV system. Thus, how to achieve desired frequency regulation with this method should be explored.

Accordingly, this paper proposes a virtual inertia control (VIC) of PV systems based on the improved PRC (MPPT-PRC) method, referring to as an event-triggering VIC. It is an extension of the work in [31]. The rest of this paper is organized as follows. Section II demonstrates the principle of the MPPT-PRC. Section III illustrates the proposed event-triggering VIC based on the MPPT-PRC. In Section IV, the proposed control method is validated by experimental tests on a real-time hardware-in-the-loop (RT-HIL) system. Finally, concluding remarks are given in Section V.

II. MPPT-Based Power Reserve Control

To achieve the PRC, the MAP (i.e., the MPP) should be identified at first, and the PRP can then be determined for power reserve operation. The general P&O-MPPT algorithm [32] is adopted to measure the MAP. Accordingly, the MPPT-PRC is achieved in this paper, which enables the event-triggering VIC of PV systems.

A. Control Principle

The main principle of the MPPT-PRC is to periodically measure the MAP by the P&O-MPPT algorithm, and then, the PRP can be obtained. As shown in Fig. 1, two operating points correspond to the same power reserve, i.e., on the left and the right side of the MPP (L-PRP and R-PRP), respectively. The PV system should operate at an assigned PRP; otherwise, the operating point may swing between L-PRP and R-PRP under disturbances, which may introduce instability. Although the PV system responds to the disturbance more sensitively at the R-PRP (i.e., fast dynamics), the PV voltage may jump to the open-circuit voltage under rapid irradiance drops. Thus, considering the stability of the system operation, the PV panels should operate at the L-PRP [33].

Reaching the desired PRP after measuring the MAP is another important issue. In [30], the P&O strategy is applied to perturb the operating point to the L-PRP gradually. However, as discussed previously, the perturbation calculation is challenging when the inertia provision is required. In this paper, the direct PV power control is adopted, where the power reserve reference is sent to the PV power controller:

$$P_{\rm pv}^{\rm PRC} = P_{\rm pv}^{\rm max} - P_{\rm res}, \tag{1}$$

in which $P_{\rm pv}^{\rm PRC}$ is the desired PV output power considering the power reserve. Then, the PI controller will regulate the PV power to follow the reference. The diagram of the MPPT-PRC is shown in Fig. 2. It shows that the MPPT-PRC incorporates two control modes, i.e., the MPPT mode and the power reserve mode. The PV system measures the MAP in the MPPT mode, while it generates the reserved power in the power reserve mode. Notably, in this method, the movement direction of the operating point cannot be specified by the PI controller. For this, a pseudo monotonic P-V curve is employed in this paper to make the PV system operate at the L-PRP, which will be discussed in Section II.B. Additionally, the control mode

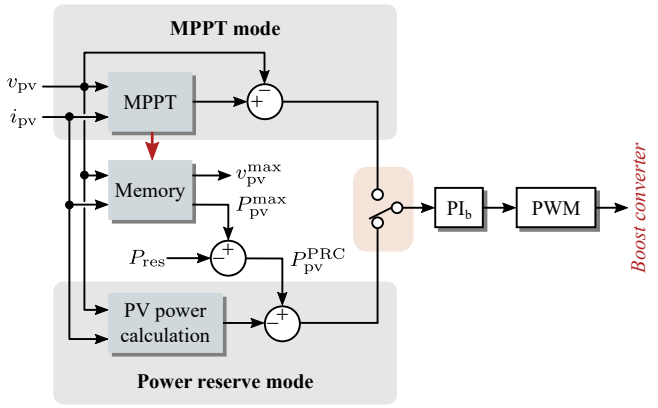

Fig. 2. Control diagram of the MPPT-PRC, where v_{pv} and i_{pv} are the PV current and voltage, and PI_b denotes the PI controller in the boost converter (PWM−pulse-width modulation).

switching is realized by an event-triggering signal, which will be presented in Section III.

The principle of the MPPT-PRC based on direct PV power control is illustrated in Fig. 3. In Fig. 3(a), two sequential PRC cycles under an increasing irradiance condition are presented to demonstrate the method. As shown in Fig. 3(a), in PRC cycle I, the MPP is tracked by the P&O-MPPT algorithm and it is denoted as MPP I. Then, the PV system is switched to the power reserve mode. The PV power controller will move the operating point to PRP I by the PI controller. Next, at the beginning of PRC cycle II, the operating point will jump from PRP I to PRP I′ due to the increasing irradiance. After that, the P&O-MPPT algorithm is enabled again. Once the operating point is perturbed to MPP II, the control system switches to the power reserve mode and the operating point will move to PRP II. Then, the PV system will wait for the next PRC cycle. The PV power controlled by the MPPT-PRC is shown in Fig. 3(b). By executing the MPPT periodically, the real-time MAP can be measured relatively accurately and the power can be efficiently reserved upon demand.

Notably, the performance of the MPPT-PRC is based on an assumption that the solar irradiance does not drastically change during the cycle transition. Otherwise, the actual MAP in the power reserve mode may differ significantly from the one measured at the beginning of each PRC cycle. This assumption holds in most cases in practice [34], e.g., for grid-scale PV systems that are usually installed in large open space. Nevertheless, the difference between the actual MAP and the measured one may be due to partial shading of PV panels even with an advanced global MPPT algorithm [35]. To alleviate this impact, the frequency of the MPPR-PRC can be increased to maintain the accuracy, or the pre-set power reserve should be increased to tolerate the difference. Alternatively, further PRC solutions and global MPPT algorithms should be developed [36], which is out of the scope of this paper. Once the MAP is obtained, the VIC is enabled for grid frequency support, which will be discussed in Section III.

B. Monotonic Power-Voltage Curve

As aforementioned, with the PI controller, the operating point in the power reserve mode may randomly settle down at

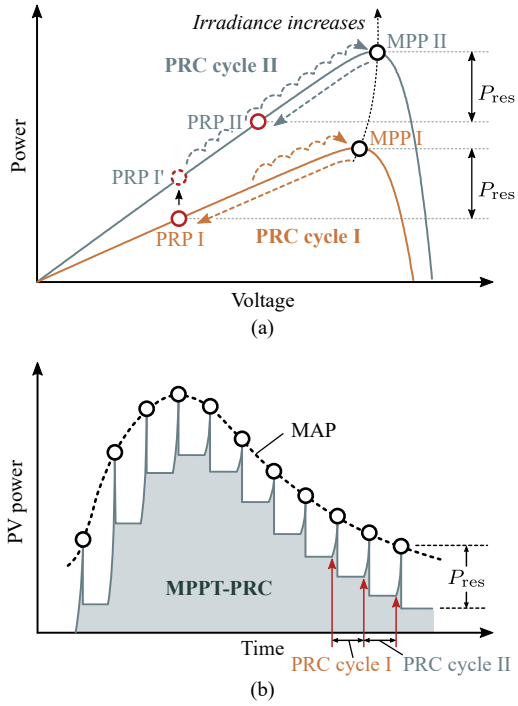

Fig. 3. Principle of the MPPT-PRC: (a) Power-voltage (P-V) curves of the PV systems in two PRC cycles and (b) PV power with the MPPT-PRC.

either the L-PRP or the R-PRP, as they are corresponding to the same power reference. To make sure that the PV system will operate at the L-PRP, the pseudo monotonic P-V curve of the PV system [27] is applied in this paper. The pseudo monotonic P-V curve is illustrated in Fig. 4. It shows that the P-V curve at the right side of the MPP is vertically mirrored with respect to the maximum power. This can be described as

$$P'_{pv} = \begin{cases} P_{pv}, & v_{pv} \le v_{pv}^{max} \\ 2P_{pv}^{max} - P_{pv}, & v_{pv} > v_{pv}^{max} \end{cases}, \tag{2}$$

where $P_{pv} = v_{pv} i_{pv}$ and P'_{pv} are the real PV power and the mirrored PV power. Then, the P-V curve in the full range of the PV voltage becomes monotonic, as shown in Fig. 4, which can then be sent to the PI controller to achieve PRC operation. In this case, when the PV system is operating at the right side of the MPP, e.g., at the R-PRP, the pseudo monotonic P-V curve will send false information to the controller for the boost converter that the actual PV power is higher than its reference. Thus, the power controller will make the operating point move to the L-PRP, where the PV output power reaches its reference. With the pseudo monotonic P-V curve, the PV power calculation block in Fig. 2 is represented by (2).

C. Transient Power Damping Control

Notably, another issue is that the P&O-MPPT algorithm inevitably introduces undesired transient power pulses when measuring the MAP, as shown in Fig. 3(b). The transient power should be properly damped to ensure the PV power quality. To buffer the excessive pulsation energy, an additional control loop is implemented in the DC-link voltage controller, being the transient power damping control (TPDC) [31]. The effect

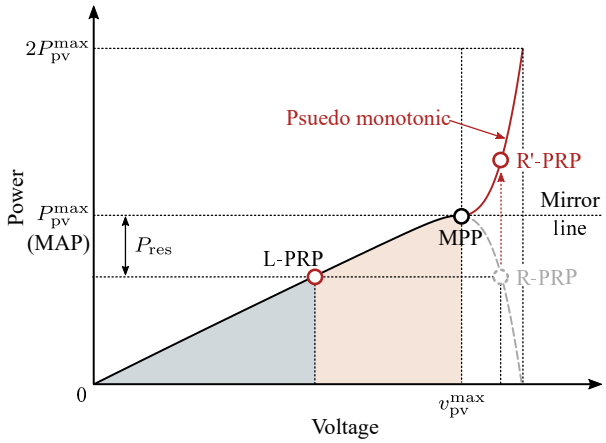

Fig. 4. Pseudo monotonic P-V curve of PV panels to ensure that the system is operating at the L-PRP, where the R′-PRP is the mirrored operating point corresponding to the R-PRP on the real P-V curve.

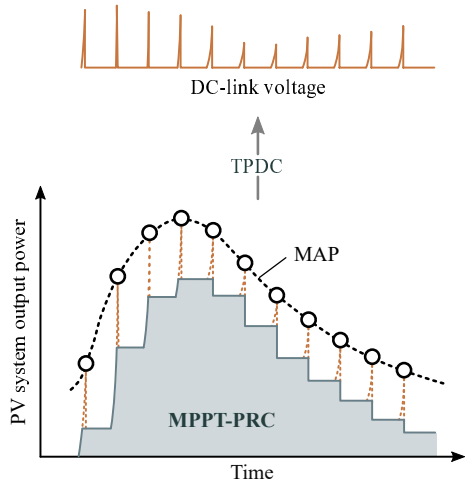

Fig. 5. Transient power damping control (TPDC) in the MPPT-PRC.

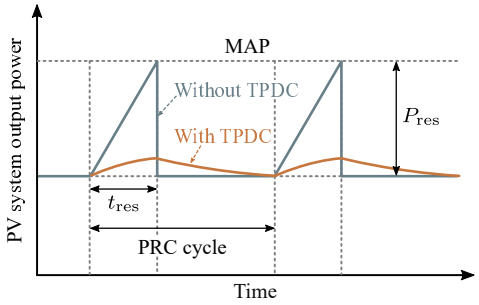

Fig. 6. Transient power during the MAP measurement with and without the TPDC, where $t_{\rm res}$ is the time duration of the MAP measurement.

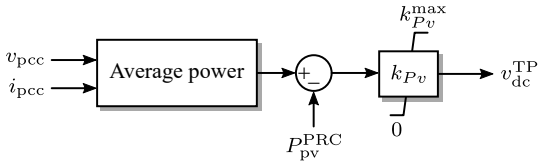

Fig. 7. Control diagram of the TPDC, where $v_{\rm pcc}$ and $i_{\rm pcc}$ are the voltage and the current at the point of common coupling (PCC), k_{Pv} is the control gain of the transient power damped by the DC-link voltage with $k_{Pv}^{\rm min}$ and $k_{Pv}^{\rm max}$ being its lower and upper limits, respectively, and $v_{\rm dc}^{\rm TP}$ is the additional DC-link voltage reference for the TPDC.

of the TPDC on the PV system output power is illustrated in Fig. 5. With the TPDC, the excessive PV system output power will be transferred to and stored in the DC-link capacitor and then released to the grid gradually. As a result, the DC-link voltage will increase, and the transient power pulses can be effectively damped. At the grid side, the PV system output power becomes much smoother, as shown in Fig. 6.

The control diagram of the TPDC is demonstrated in Fig. 7. The difference between the actual PV system output power and the reserved PV power reference is adopted to generate the additional DC-link voltage reference (in addition to the basic DC-link voltage reference). Notably, the power-voltage control gain k_{Pv} is of importance for the TPDC performance. When k_{Pv} is large, the DC-link voltage can deviate largely from the rated value to buffer the transient power. However, the DC-link voltage deviation is limited by the operation requirements, e.g., the capacitor lifetime, the modulation requirement, the converter stability, etc. In this regard, k_{Pv} should be constrained by the DC-link voltage deviation limitation and the transient power. Additionally, the proportional gain of the DC-link voltage controller should be considered, as it affects the response time of the DC-link voltage. In an extreme case, the DC-link voltage deviates to its limit to buffer the transient power, which is approximately equal to the power reserve. Accordingly, the maximum k_{Pv} can be calculated by

$$k_{Pv}^{\rm max} = \frac{v_{\rm dc}^{\rm max} - v_{\rm dc}^{*}}{P_{\rm res}} \cdot \frac{1}{k_{\rm pdc}}, \tag{3}$$

where $v_{\rm dc}^{\rm max}$ is the maximum allowable DC-link voltage, $v_{\rm dc}^{*}$ is the DC-link voltage reference, $k_{\rm pdc}$ is the proportional coefficient of the DC-link voltage controller, and $k_{Pv}^{\rm max}$ is the upper limit of k_{Pv}.

It should be mentioned that the requirement of transient power damping is not considered when designing the DC-link capacitor in a conventional system. That is, the amount of the power reserve is limited by the pre-designed DC-link capacitor and DC-link voltage deviation limitation. The maximum energy stored in the DC-link capacitor during the MAP measurement can be calculated as

$$E_{\rm dc}^{\rm max} = \frac{1}{2} C_{\rm dc} [(v_{\rm dc}^{\rm max})^2 - (v_{\rm dc}^{*})^2], \tag{4}$$

where $E_{\rm dc}^{\rm max}$ is the maximum energy stored in the DC-link voltage during the MPPT operation in a PRC cycle and $C_{\rm dc}$ is the DC-link capacitance.

On the other hand, according to Fig. 6, the transient energy generated by the MAP measurement can be calculated as

$$E_{\rm res} = \frac{1}{2} P_{\rm res} t_{\rm res}, \tag{5}$$

in which $t_{\rm res}$ is the time duration of the MAP measurement. It is determined by the amount of the power reserve and the MPPT algorithm. Based on (4) and (5), making $E_{\rm dc}^{\rm max} = E_{\rm res}$ leads to

$$P_{\rm res}^{\rm max} = \frac{C_{\rm dc}}{t_{\rm res}} [(v_{\rm dc}^{\rm max})^2 - (v_{\rm dc}^{*})^2], \tag{6}$$

with $P_{\text{res}}^{\max}$ being the maximum power reserve considering the DC-link capacitor voltage withstanding capability.

III. Event-Triggering Virtual Inertia Control

The MPPT-PRC can reserve a certain amount of power for PV systems. Then, the flexible active power control of PV systems, including the VIC, becomes possible. However, the specific realization of the VIC has not been discussed in the literature. In the PRC methods depending on sensors, curve-fitting algorithms, empirical models, or master-slave PV system configurations, the MAP estimation can be independently realized. Thus, the design of the VIC can be decoupled with the PRC method to some extent. On the contrary, in the MPPT-PRC method, the power reserve is based on the measured MAP. Then, the MAP measurement loop couples with the power reserve loop. For instance, the MAP measurement cannot be activated with the VIC simultaneously; otherwise, the control loops may conflict with each other, and instability may appear. As a result, the coordination of the MPPT-PRC and the VIC should be considered, which will be presented in this section.

A. Virtual Inertia Control of PV Systems

As discussed Section I, for RESs, the SG characteristics can be mimicked in a way to provide inertia. The swing equation of an SG rotor is expressed as

$$\begin{cases} P_{\text{m}} - P_{\text{e}} - D(\omega - \omega_0) = 2H\dfrac{d\omega}{dt} \\ \dfrac{d\theta}{dt} = \omega - \omega_0 \end{cases}, \tag{7}$$

with P_{m} and P_{e} being the mechanical power and the electromagnetic power of the SG, respectively, H and D being the inertia constant and damping coefficient, ω being the angular frequency, ω_0 being the rated frequency, and θ being the internal voltage phase angle of the SG.

It can be seen from (7) that the inertia determines the proportional relationship between the active power and the derivative of the frequency, i.e., the rate of change of frequency (RoCoF). Thus, to emulate the inertia in PV systems, the PV output power to the grid should be proportional to the RoCoF, i.e.,

$$P_{\text{pv}}^{\text{VIC}} = 2H_{\text{pv}}\frac{d\omega}{dt}, \tag{8}$$

where $P_{\text{pv}}^{\text{VIC}}$ is an additional PV power reference for the controller in the boost converter and H_{pv} is the virtual inertia of the PV system that provides.

Notably, since the PV system output power performs as the additional electromagnetic power for the frequency governor, i.e., the SG, the control gain from the RoCoF to the PV power reference should be inversely proportional. Thus, the additional power reference $P_{\text{pv}}^{\text{VIC}}$ should be negative when being added to the controller for the boost converter. Moreover, the virtual inertia of the PV system is limited by the amount of the power reserve. By assuming that all the power reserve is used to provide the virtual inertia, the maximum virtual inertia can be obtained as

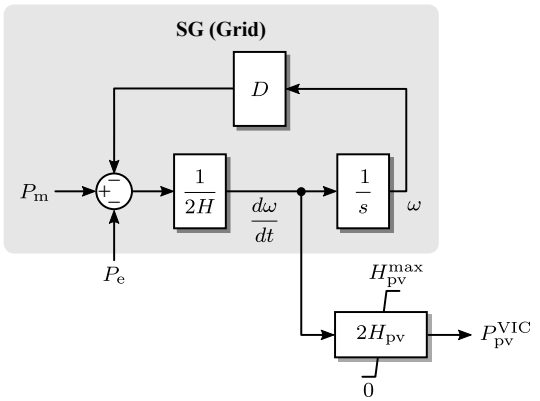

Fig. 8. Diagram of the VIC for PV systems, where $H_{\text{pv}}^{\max}$ is the upper limit of the virtual inertia provided by the PV systems.

$$H_{\text{pv}}^{\max} = \frac{P_{\text{res}}/P_{\text{rated}}}{2\dfrac{d\omega_{\text{t}}}{dt}/\omega_0}, \tag{9}$$

where $\dfrac{d\omega_{\text{t}}}{dt}$ is the RoCoF threshold, and P_{rated} is the rated PV power at standard test condition (STC). In this paper, the RoCoF threshold is the RoCoF withstanding capability of power generation units defined in grid codes [8].

The diagram of the proposed VIC for PV systems is presented in Fig. 8, where the operation of the grid (represented by an SG) follows the swing equation given in (7). Notably, in a real power grid, the RoCoF is provided by the system operator, whereas it is measured in the SG in Fig. 8 for illustration. It should be mentioned that the RoCoF for the VIC of the PV systems can be also calculated based on the frequency measured through a phase-locked loop (PLL) or a frequency-locked loop (FLL). However, the derivative calculation introduces significant noise and errors into the controller. Other advanced frequency and RoCoF measurement methods may be employed [37], which, however, is out of the scope of this paper.

B. Event-Triggering Signal

Due to the coupling of the MPPT-PRC and the power reserve loop, they cannot be designed independently. They should be coordinated in harmony to avoid conflict and potential instability of the PV systems. In this context, the coordination between the VIC and the MPPT-PRC is important for the VIC performance. An event-triggering strategy is then introduced into the aforementioned control system to achieve the control system coordination. It is in charge of the operational mode switching between the MPPT mode and the power reserve mode in the PRC. Moreover, the control signal activates the VIC when it is required by the grid. To achieve these functionalities, the operation logic of the event-triggering signal should be adequately designed. Basically, the PV system will operate in the MPPT mode when the event-triggering signal is "1" and in the power reserve mode when

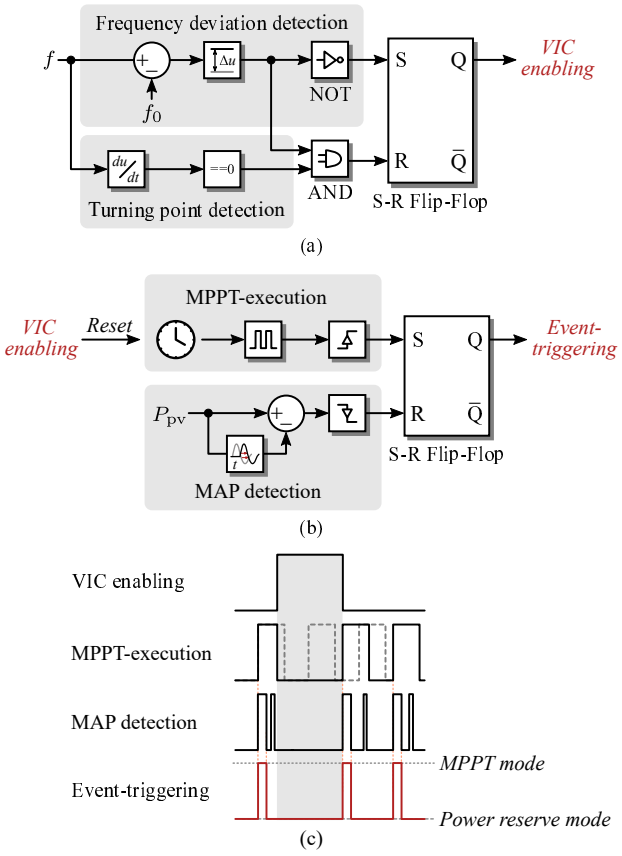

Fig. 9. Operation logic of the event-triggering control strategy: (a) generation of the VIC enabling signal, (b) generation of the event-triggering signal, and (c) example waveform of the signals, where f and f_0 are the actual grid frequency and the rated grid frequency.

it is "0". According to Fig. 9, the generation of the event-triggering signal is summarized as:

- *MPPT-execution signal*: A periodical square-wave is adopted to periodically trigger the MPPT, as discussed in Section II. Specifically, each rising edge of the square-wave sends "1" to the S-port of an S-R flip-flop, which makes the event-triggering signal turn to "1". Then, the PV system will operate in the MPPT mode.
- *MAP detection signal*: Once the MAP is measured, the MAP detection signal will be changed from "1" to "0", which produces a falling edge. Every falling edge sends "1" to the R-port of the S-R flip-flop. Then, the event-triggering signal jumps from "1" to "0". Consequently, the PV system will transit to the power reserve mode.
- *VIC enabling signal*: Once the frequency exceeds the limits set by the system operator, the VIC should be activated. Then, when the frequency returns to the steady-state (i.e., the nominal frequency range), the VIC can be disabled. Specifically, if the frequency deviation from the rated is within the limits when the RoCoF equals to zero, the frequency is considered to be in the steady-state. When the VIC enabling signal is negative, the VIC control loop is disabled, and the PV system is controlled by the periodical MPPT-PRC to continuously reserve the power. When inertia is required by the grid, the VIC signal is positive to enable the inertia provision. In this case, the MPPT-PRC will be provisionally deactivated until the frequency returns to the steady-state. In addition, the TPDC in the grid-connected inverter is disabled as well during the VIC operation.

Notably, it is difficult to predict the MAP detection signal in the power reserve mode, as the PV output power may be controlled to be constant or varying for grid support, which makes the MAP detection signal jump between "0" and "1". Thus, the MAP detection signal should be reset to be "1" by every rising edge of the MPPT-execution signal to ensure that an effective falling edge can be generated once the MAP is measured. In all, the event-triggering signal turns to "1" periodically with the rising edges of the MPPT-execution signal, and turns to "0", when the MAP is measured in every PRC cycle. Additionally, when the VIC enabling signal is activated, the event-triggering signal remains "0" and will be reset once the VIC enabling signal turns back to "0".

C. Coordinated Control System

The diagram of the entire coordinated control system is shown in Fig. 10, where a two-stage three-phase PV system is considered. In Fig. 10, the boost converter is responsible for the PV power regulation using a PI controller (i.e., PI_b in Fig. 10), where the PV system operates in the MPPT mode or the power reserve mode. When the PV system is operating in the power reserve mode, the VIC can be implemented to regulate the PV power in response to the grid frequency deviation. With the VIC, the PV power reference in the power reserve mode is changed from P_pv^PRC to $P_\text{pv}^\text{PRC} - P_\text{pv}^\text{VIC}$, as shown in Fig. 10. The dual-loop control strategy is adopted in the grid-connected inverter, where the PI-based (i.e., PI_dc in Fig. 10) DC-link voltage control is applied as the outer control loop. Moreover, the TPDC is implemented to make the DC-link capacitor performs as a buffer when needed, e.g., when the transient power produced in the MPPT operation needs to be absorbed, as discussed in Section II.C.

IV. Experimental Results

The proposed MPPT-PRC-based VIC method is validated on an RT-HIL system with a StarSim field-programmable gate array (FPGA) Solver and StarSim HIL, where the circuit is implemented on a NI-PXIe-FPGA-7868R board. The controller is implemented on a NI-PXIe-FPGA-7846R board. The experimental platform is shown in Fig. 11. A two-stage three-phase PV system is developed referring to Fig. 10, of which the parameters are given in Table I. Notably, the PV panel includes 3 strings (each has 10 PV modules of 305 W), corresponding to the total power of 9.2 kW at standard test condition (STC).

A. Performance of The MPPT-PRC Strategy

A constant solar irradiance level of 1000 W/m^2 and a constant temperature of 25 °C are considered, where the PRC period is 6 s (see [30] for more information on the PRC period selection). Considering the maximum DC-link voltage deviation as 10% and t_res as 0.5 s, the maximum power reserve

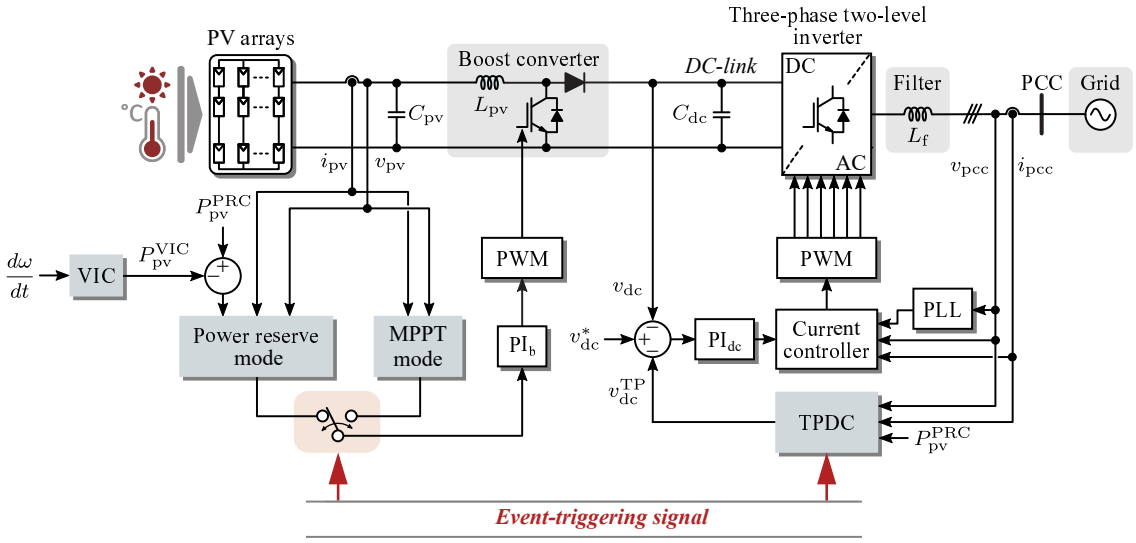

Fig. 10. Diagram of the entire coordinated control system of a two-stage three-phase PV system with the proposed MPPT-PRC-based VIC, where C_{pv} is the boost capacitor, L_{pv} and L_f are the boost inductance and the inverter filter inductance, v_{pv}^* is the PV voltage reference, v_{dc} and v_{dc}^* are the DC-link voltage and its reference (PLL—phase-locked loop).

is calculated to be approximately 1.2 kW according to (6). The required power reserve is set to be 1 kW (10% of the rated) in the case study.

First, the MPPT-PRC without the TPDC is performed. The system dynamics are shown in Fig. 12. It can be seen in Fig. 12(a) that the event-triggering signal is regularly changing to either "0" or "1", making the PV system operate in the MPPT mode and the power reserve mode. More specifically, the MPPT-execution signal (50% square wave) turns to "1" at the beginning of every PRC cycle, which simultaneously activates the MPPT detection signal and the event-triggering signal, and the PV system is controlled by the P&O-MPPT algorithm. Once the MAP is detected, the MAP detection signal turns to "0" from "1", which makes the event-triggering signal turn to "0". Then, the PV system switches to the power reserve mode. In addition, when the MPPT-execution signal is "0", the MAP detection signal is disabled, e.g., it is compulsively set to be "0". This ensures that the MAP detection function is available in the next PRC cycle. Seen from Fig. 12(b), the MPPT-PRC performs well to measure the MAP. Once the MAP is detected, the event-triggering signal turns to "0" and the PV system immediately switches to the power reserve mode, where the PV system output falls to 8.2 kW with fast dynamics. However, the MPPT operation inevitably generates transient power, the peak of which approximately equals to the power reserve, i.e., 1 kW in this case. If the TPDC is not applied, the DC-link capacitor is not regulated to buffer the transient energy (see Fig. 12(c)), and the significant transient power pulses will be delivered to the grid, yielding poor-quality PV power generation, as shown in Fig. 12(b).

The performance of the MPPT-PRC with the TPDC is then performed. The maximum TPDC control gain $k_{Pv}^{\max}$ can be calculated as 10 according to (3), and 5 is selected in this paper as the TPDC gain. The system dynamics are shown in Fig. 13. It can be seen in Fig. 13 that the MPPT-PRC with the TPDC

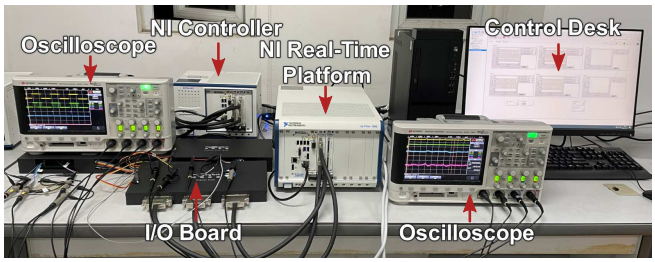

Fig. 11. RT-HIL experimental system.

TABLE I
PARAMETERS OF THE TWO-STAGE THREE-PHASE PV SYSTEM.

Parameter	Description	Value
P_{rated}	Inverter rated power	10 kW
v_{dc}^*	DC-link voltage reference	700 V
v_{ac}	Rated grid voltage (line-to-line RMS)	400 V
f_b	Boost converter switching frequency	10 kHz
f_{inv}	Inverter switching frequency	10 kHz
f_{MPPT}	MPPT sampling frequency	100 Hz
f_0	Rated grid frequency	50 Hz
L_{pv}	Boost converter inductance	1 mH
L_f	Inverter filter inductance	6 mH
C_{pv}	Boost converter capacitor	470 μF
C_{dc}	DC-link capacitor	5600 μF
(k_{pb}, k_{ib})	Boost converter PI controller parameters, PI_b	(2, 80)
(k_{pdc}, k_{idc})	DC-link voltage PI controller parameters, PI_{dc}	(0.1, 1)

can also effectively coordinate the MPPT mode and the power reserve mode. Additionally, the DC-link capacitor participates more in the power regulation. When the PV system output power exceeds the reference with the reserve, indicating the PV system turns into the MPPT mode and the transient power is being generated, the DC-link capacitor increases the voltage to absorb the transient power. With an adequately designed

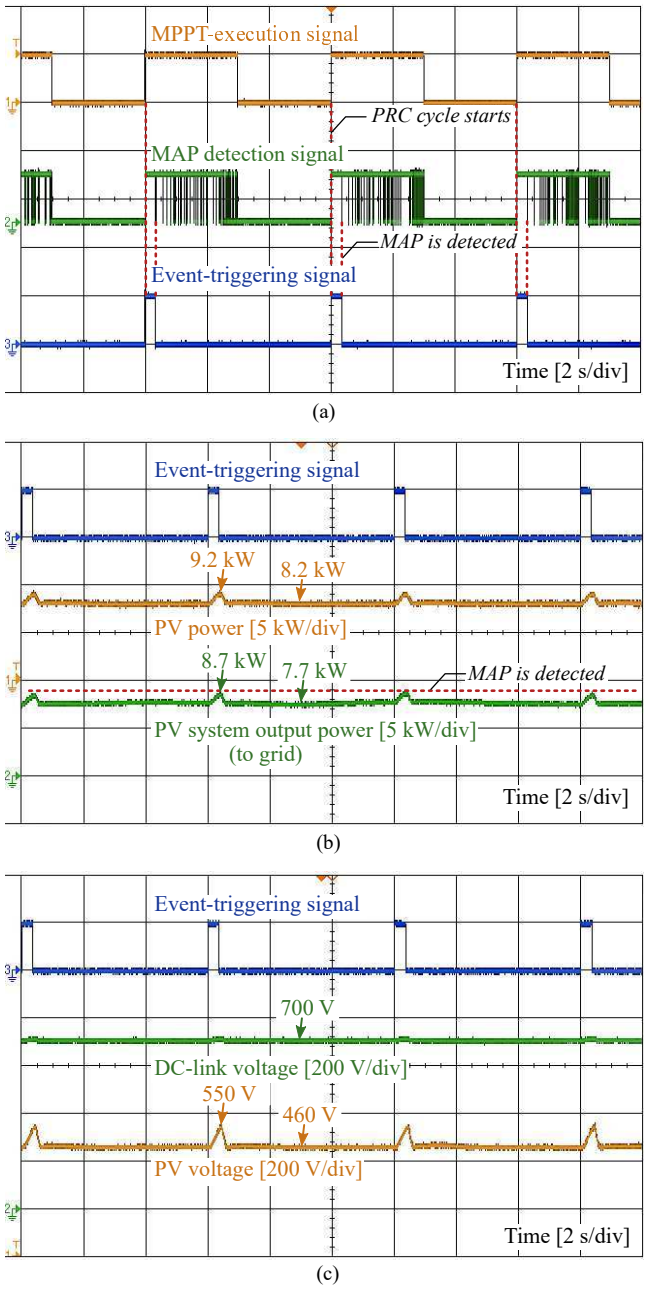

Fig. 12. Performance of the two-stage PV system with the MPPT-PRC, where the TPDC is disabled, under a constant irradiance and temperature condition: (a) control signals, (b) active power, and (c) voltage.

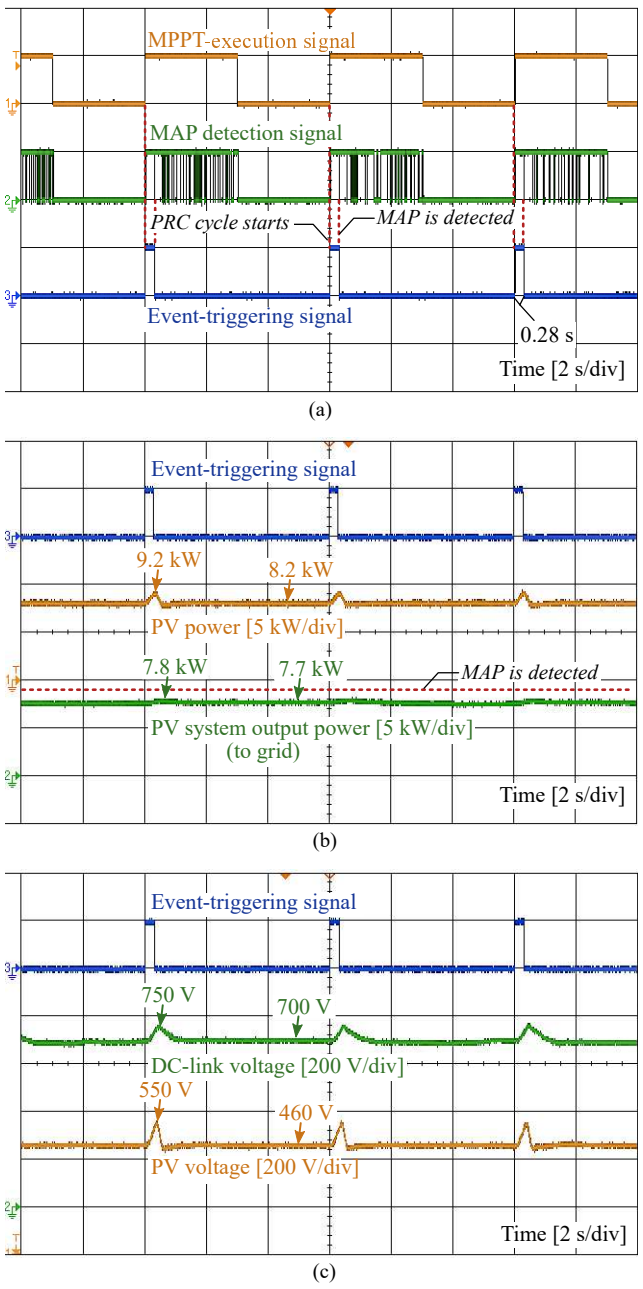

Fig. 13. Performance of the two-stage PV system with the MPPT-PRC, where the TPDC is enabled, under a constant irradiance and temperature condition: (a) control signals, (b) active power, and (c) voltage.

TPDC control gain k_{Pv}, the DC-link voltage deviation during the transients does not exceed the defined margin, i.e., less than 10%, while the transient power is effectively damped to 0.1 kW (1% of the rated power). That is, the PV system output power to the grid is smoothed to a large extent by the TPDC, as shown in Fig. 13. The smooth power output ensures the system stability, and more importantly, it lays a solid foundation for the VIC. Notably, the time duration of the MAP measurement, t_{res}, is around 0.28 s, which is much smaller than 0.5 s. Thus, applying $t_{\text{res}} = 0.5$ s to calculate the maximum power reserve is reasonable and reliable.

B. Performance of The Strategy Under Irradiance Changes

To validate the performance of the MPPT-PRC under varying environmental conditions, the experiments under irradiance changes are conducted, while the ambient temperature remains unchanged. In the initial state, the irradiance is 1000 W/m^2. Then, the irradiance is gradually reduced to 600 W/m^2. The system dynamics are shown in Fig. 14. It can be observed in Fig. 14 that the MAP decreases with the falling irradiance. The MPPT-PRC method can accurately measure the MAP with constant and varying irradiance. In such a case, the power reserve points can be accurately identified, and the PV system output power can be effectively shaped with the desired power

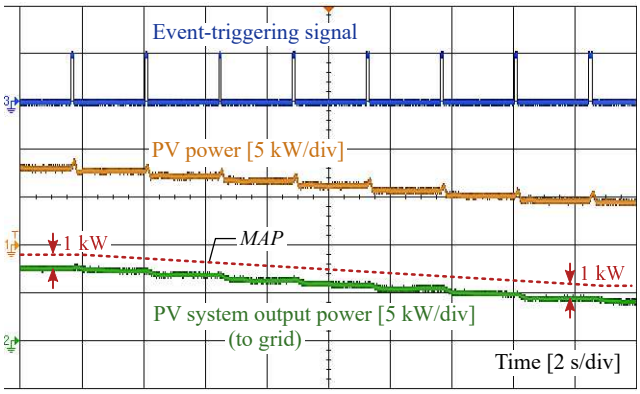

Fig. 14. Performance of the two-stage PV system with the MPPT-PRC, where the TPDC is enabled under irradiance change. Here, the power reserve of 1 kW is maintained.

TABLE II
PARAMETERS OF THE VSG REPRESENTING THE GRID IN FIG. 10.

Parameter	Description	Value
P^{g}	Power rating	10 kW
$v^{\mathrm{g}}_{\mathrm{rated}}$	Rated line-to-line grid voltage	400 V
$v^{\mathrm{g}}_{\mathrm{dc}}$	Rated DC-link voltage	800 V
R	Speed regulation gain of governor	0.05 p.u.
T_{G}	Governor time constant	0.2 s
T_{T}	Turbine time constant	0.3 s
H	Inertia constant	5 s
D	Damping coefficient	1 p.u.
f_0	Rated frequency	50 Hz
$L^{\mathrm{inv}}_{\mathrm{f}}$	Converter-side filter inductance	4.8 mH
$L^{\mathrm{g}}_{\mathrm{f}}$	Grid-side filter inductance	2 mH
$C^{\mathrm{g}}_{\mathrm{f}}$	Filter capacitance	10 μF

reserve. It can also be seen in Fig. 14 that with the TPDC, the transient power generated during the MPPT operation can be effectively damped, and the PV system output power to the grid is smoothed. Additionally, when the irradiance decreases, the PV system operating point at the end of a PRC cycle moves closer to the MPP for the next PRC cycle, which reduces the steps to measure the MAP. As a result, the transient power generated by the MPPT operation becomes smaller. In all, the MPPT-PRC, including the TPDC, performs well when the irradiance changes.

C. Performance of The VIC Based on The MPPT-PRC

The MPPT-PRC has been validated to be effective to allow the PV system to operate in the power reserve mode. Based on the MPPT-PRC, the performance of the proposed VIC is validated on the two-stage three-phase PV system. Notably, to obtain the system frequency response, a virtual synchronous generator (VSG) is applied in the system to represent the grid, of which the parameters are shown in Table II. When a 1.8 kW (10%) load step is applied in the system and then cleared, the system dynamics without VIC of the PV system are shown in Fig. 15. It can be observed that the PV system does not respond to the load step when the VIC is disabled. In this case, the frequency drops to 49.4 Hz after the load step, where the RoCoF reaches –0.86 Hz/s.

The experimental test of the MPPT-PRC-based VIC is then performed. According to (9), with the RoCoF threshold being 1 Hz/s (comprehensively considering the RoCoF withstanding requirements in various grid codes [8], [38]), the maximum allowed virtual inertia emulated by the PV system is $H^{\mathrm{max}}_{\mathrm{pv}}$ = 2.5 s. With the maximum virtual inertia, the control signals and the system dynamics under a 10%-load step are shown in Fig. 16. It can be seen from Fig. 16 that the proposed VIC can effectively detect the grid frequency deviation and provide sufficient frequency support to the grid, which adequately coordinates the VIC with the MPPT-PRC. Specifically, as shown in Fig. 16(a), after the load steps, the grid frequency deviation quickly exceeds the limit ($\pm$0.1 Hz in this paper), and the VIC enabling signal turns to "1", indicating the frequency instability issue is detected. Once the VIC enabling signal turns to "1", the PV system continuously operates in the power reserve mode with the VIC being triggered, and the MPPT-PRC is temporarily disabled. In this case, when the next MPPT-PRC cycle begins if the VIC is not triggered, the MPPT-execution signal will not turn to "1" to activate the MPPT algorithm due to the VIC enabling signal. Instead, the PV system stays in the power reserve mode and regulates the output power to provide the grid frequency support until the frequency reaches the steady-state, i.e., the frequency deviated from the rated within the limit ($\pm$0.1 Hz in this paper) when the RoCoF is almost zero. Then, the VIC enabling signal turns back to "0", and the MPPT-PRC is triggered again by resetting the MPPT-execution signal, as shown in Fig. 16(a). As a result, the MPPT-execution signal is delayed, and the delay is affected by the duration of the frequency instability issues. After that, the PV system returns to periodically switch between the MPPT and the power reserve modes.

The PV system dynamics are shown in Fig. 16(b). When the VIC enabling signal turns to "1" following the load step, the VIC is triggered, and the PV system starts to regulate its output power in proportion to the RoCoF. When the load step is cleared, the PV system continues to regulate the output power until the frequency goes back to the steady-state. Then, the VIC is disabled and the MPPT-PRC is reset, which makes the PV system execute the MPPT algorithm again to measure the MAP. It can be seen from Fig. 16(b) that the periodical transient power generated by the MPPT operation is delayed due to the VIC. As for the frequency support, the PV system increases about 0.9 kW output power at the beginning of the frequency incident, where the RoCoF is at the largest level during the transient. With the VIC of the PV system, the frequency nadir increases to 49.5 Hz, indicating a 16.7% reduction of the peak frequency deviation compared with the case without the VIC. Moreover, The RoCoF after the load step decreases by 5.8% from –0.86 Hz/s to –0.81 Hz/s. Notably, the RoCoF after the load step has not been significantly reduced. This is due to that the frequency incident is detected and the VIC of PV system is activated once the frequency exceeds the limit, instead of the load step point. When the VIC is enabled, the RoCoF is reduced effectively. For instance, after the load step is cleared, the RoCoF decreases by 20% from 0.9 Hz/s to 0.72 Hz/s. Overall, the MPPT-PRC and the VIC of the

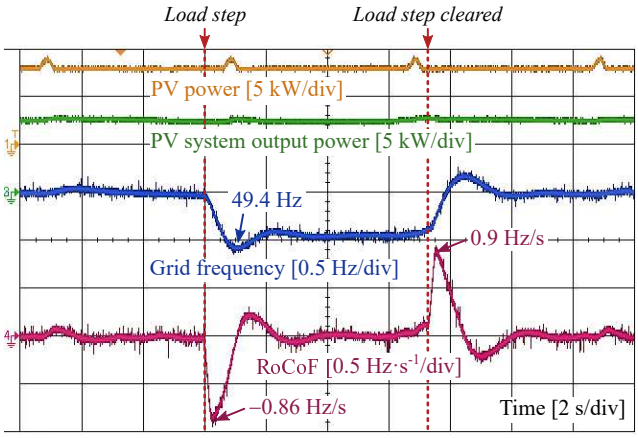

Fig. 15. Dynamic performance of the two-stage PV system without the VIC under a load step.

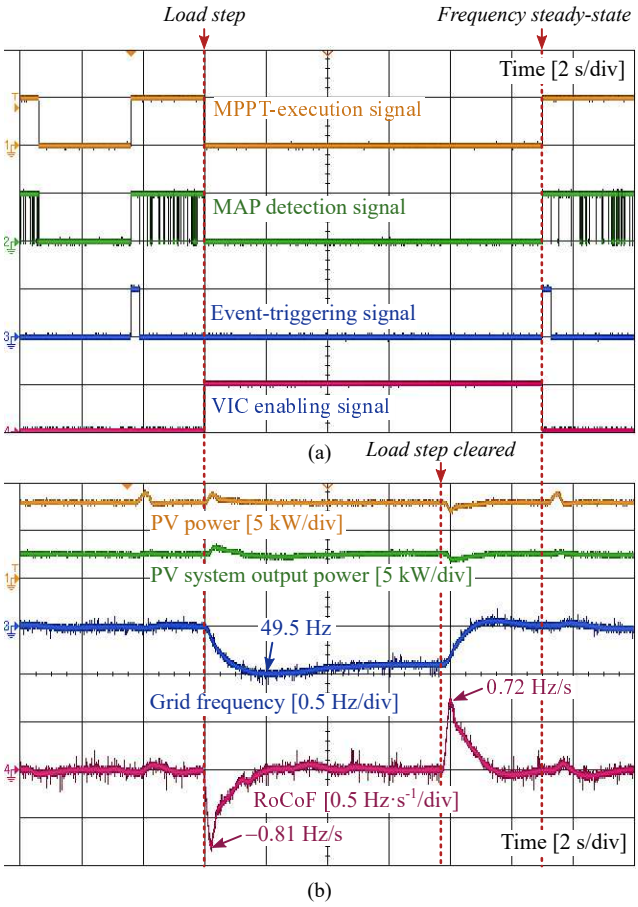

Fig. 16. Dynamic performance of the two-stage PV system with the proposed VIC based on the MPPT-PRC under a load step: (a) control signals and (b) power and frequency.

PV system is effectively coordinated, and the grid frequency quality is improved with the support from the PV system by the proposed method.

V. Conclusion

An event-triggering VIC based on the MPPT-PRC for two-stage three-phase PV systems was proposed in this paper. Firstly, the MPPT-PRC is applied to achieve the power reserve of PV systems. The MPPT-PRC is cost-effective and computational-efficient, as it does not require communication, sensors, or curve-fitting algorithms. A pseudo monotonic P-V curve makes the PV system operate at the L-PRP. A TPDC method effectively buffers the transient power impulses due to the MAP measurement. Based on the PRC, various ancillary grid support control scheme can be realized, including the VIC. An event-triggering signal was proposed in this paper to coordinate the MPPT-PRC and the VIC. Accordingly, different control modes of PV systems are effectively organized. As a consequence, conflicts during the mode switching are avoided and the system stability is maintained. The proposed control was validated by experimental tests. In the future, in addition to the VIC, the MPPT-PRC can be used to provide more ancillary support to the grid from PV systems, based on which a smarter and more flexible power system can be expected.

Acknowledgment

The authors would like to thank Dr. Junpeng Ma and Mr. Lin Feng from Sichuan University for the support in developing the tests on the RT-HIL system.

References

[1] IRENA, "Global Eergy Transformation: A Roadmap to 2050 (2019 Edition)," Abu Dhabi, UAE, Tech. Rep. ISBN: 978-92-9260-121-8, Apr. 2019.
[2] SolarPower Europe, "Global Market Outlook for Solar Power 2020-2024," Brussels, Belgium, Tech. Rep., Jun. 2020.
[3] AEMO, "Black System South Australia 28 September 2016 - Final Report," Tech. Rep., Mar. 2017.
[4] National Grid ESO, "Technical Report on the Events of 9 August 2019," Wokingham, UK, Tech. Rep., Sep. 2019.
[5] IEEE Std 1547-2018 Revis. IEEE Std 1547-2003, *IEEE Standard for Interconnection and Interoperability of Distributed Energy Resources with Associated Electric Power Systems Interfaces*. New York, NY, USA: IEEE, Apr. 2018.
[6] Hydro-Quebéc, "Technical Requirements for the Connection of Generating Stations to the Hydro-Québec Transmission System," Montréal, QC, Canada, Tech. Rep. Decision D-2018-145, Jan. 2019.
[7] T.-T. Ku, C.-H. Lin, C.-T. Hsu, C.-S. Chen, Z.-Y. Liao, S.-D. Wang, and F.-F. Chen, "Enhancement of Power System Operation by Renewable Ancillary Service," *IEEE Trans. Ind. Appl.*, vol. 56, no. 6, pp. 6150–6157, Nov. 2020.
[8] J. Fang, H. Li, Y. Tang, and F. Blaabjerg, "On the Inertia of Future More-Electronics Power Systems," *IEEE J. Emerg. Sel. Top. Power Electron.*, vol. 7, no. 4, pp. 2130–2146, Dec. 2019.
[9] P. Kundur, N. J. Balu, and M. G. Lauby, *Power System Stability and Control*. New York, NY, USA: McGraw-hill, 1994.
[10] B. K. Poolla, D. Groß, and F. Dörfler, "Placement and Implementation of Grid-Forming and Grid-Following Virtual Inertia and Fast Frequency Response," *IEEE Trans. Power Syst.*, vol. 34, no. 4, pp. 3035–3046, Jul. 2019.
[11] U. Markovic, Z. Chu, P. Aristidou, and G. Hug, "LQR-Based Adaptive Virtual Synchronous Machine for Power Systems With High Inverter Penetration," *IEEE Trans. Sustain. Energy*, vol. 10, no. 3, pp. 1501–1512, Jul. 2019.
[12] Q. Peng, A. Sangwongwanich, Y. Yang, and F. Blaabjerg, "Grid-Friendly Power Control for Smart Photovoltaic Systems," *Solar Energy*, vol. 210, pp. 115–127, Nov. 2020.
[13] D. Remon, A. M. Cantarellas, J. M. Mauricio, and P. Rodriguez, "Power system stability analysis under increasing penetration of photovoltaic power plants with synchronous power controllers," *IET Renew. Power Gener.*, vol. 11, no. 6, pp. 733–741, 2017.
[14] P. Rodríguez, C. Citro, J. I. Candela, J. Rocabert, and A. Luna, "Flexible Grid Connection and Islanding of SPC-Based PV Power Converters," *IEEE Trans. Ind. Appl.*, vol. 54, no. 3, pp. 2690–2702, May 2018.

[15] R. K. Sarojini, K. Palanisamy, P. Sanjeevikumar, and J. B.-H. Nielsen, "Inertia emulation control technique based frequency control of grid-connected single-phase rooftop photovoltaic system with battery and supercapacitor," *IET Renew. Power Gener.*, vol. 14, no. 7, pp. 1156–1163, 2020.

[16] X. Lyu, Z. Xu, J. Zhao, and K. P. Wong, "Advanced frequency support strategy of photovoltaic system considering changing working conditions," *Transm. Distrib. IET Gener.*, vol. 12, no. 2, pp. 363–370, 2018.

[17] M. Dreidy, H. Mokhlis, and S. Mekhilef, "Inertia response and frequency control techniques for renewable energy sources: A review," *Renewable and Sustainable Energy Reviews*, vol. 69, pp. 144–155, Mar. 2017.

[18] C. Loutan, P. Klauer, S. Chowdhury, S. Hall, M. Morjaria, V. Chadliev, N. Milam, C. Milan, and V. Gevorgian, "Demonstration of Essential Reliability Services by a 300-MW Solar Photovoltaic Power Plant," National Renewable Energy Laboratory, Golden, CO, USA, Tech. Rep. NREL/TP-5D00-67799, Mar. 2017.

[19] A. Sangwongwanich, Y. Yang, F. Blaabjerg, and D. Sera, "Delta Power Control Strategy for Multistring Grid-Connected PV Inverters," *IEEE Trans. Ind. Appl.*, vol. 53, no. 4, pp. 3862–3870, Jul. 2017.

[20] G. Bao, H. Tan, K. Ding, M. Ma, and N. Wang, "A Novel Photovoltaic Virtual Synchronous Generator Control Technology Without Energy Storage Systems," *Energies*, vol. 12, no. 12, p. 2240, Jun. 2019.

[21] Vahan Gevorgian, "Highly Accurate Method for Real-Time Active Power Reserve Estimation for Utility-Scale Photovoltaic Power Plants," National Renewable Energy Laboratory, Golden, CO, USA, Tech. Rep. NREL/TP-5D00-73207, Feb. 2019.

[22] A. F. Hoke, M. Shirazi, S. Chakraborty, E. Muljadi, and D. Maksimovic, "Rapid Active Power Control of Photovoltaic Systems for Grid Frequency Support," *IEEE J. Emerg. Sel. Top. Power Electron.*, vol. 5, no. 3, pp. 1154–1163, Sep. 2017.

[23] B. Crăciun, T. Kerekes, D. Séra, and R. Teodorescu, "Frequency Support Functions in Large PV Power Plants With Active Power Reserves," *IEEE J. Emerg. Sel. Top. Power Electron.*, vol. 2, no. 4, pp. 849–858, Dec. 2014.

[24] X. Chen, Y. Du, H. Wen, L. Jiang, and W. Xiao, "Forecasting-Based Power Ramp-Rate Control Strategies for Utility-Scale PV Systems," *IEEE Trans. Ind. Electron.*, vol. 66, no. 3, pp. 1862–1871, Mar. 2019.

[25] S. I. Nanou, A. G. Papakonstantinou, and S. A. Papathanassiou, "A Generic Model of Two-Stage Grid-Connected PV Systems with Primary Frequency Response and Inertia Emulation," *Electr. Power Syst. Res.*, vol. 127, pp. 186–196, Oct. 2015.

[26] X. Huang, K. Wang, G. Li, and H. Zhang, "Virtual Inertia-Based Control Strategy of Two-Stage Photovoltaic Inverters for Frequency Support in Islanded Micro-Grid," *Electronics*, vol. 7, no. 11, p. 340, Nov. 2018.

[27] E. I. Batzelis, G. E. Kampitsis, and S. A. Papathanassiou, "Power Reserves Control for PV Systems With Real-Time MPP Estimation via Curve Fitting," *IEEE Trans. Sustain. Energy*, vol. 8, no. 3, pp. 1269–1280, Jul. 2017.

[28] X. Li, H. Wen, Y. Zhu, L. Jiang, Y. Hu, and W. Xiao, "A Novel Sensorless Photovoltaic Power Reserve Control With Simple Real-Time MPP Estimation," *IEEE Trans. Power Electron.*, vol. 34, no. 8, pp. 7521–7531, Aug. 2019.

[29] C. Zhong, Y. Zhou, and G. Yan, "Power reserve control with real-time iterative estimation for PV system participation in frequency regulation," *International Journal of Electrical Power & Energy Systems*, vol. 124, p. 106367, Jan. 2021.

[30] A. Sangwongwanich, Y. Yang, and F. Blaabjerg, "A Sensorless Power Reserve Control Strategy for Two-Stage Grid-Connected PV Systems," *IEEE Trans. Power Electron.*, vol. 32, no. 11, pp. 8559–8569, Nov. 2017.

[31] Q. Peng, Z. Tang, Y. Yang, and F. Blaabjerg, "Event-Triggering Power Reserve Control for Grid-Connected PV Systems," in *Proc. IEEE APEC 2020*, Mar. 2020, pp. 417–423.

[32] T. Esram and P. L. Chapman, "Comparison of Photovoltaic Array Maximum Power Point Tracking Techniques," *IEEE Trans. Energy Convers.*, vol. 22, no. 2, pp. 439–449, Jun. 2007.

[33] Y. Yang, H. Wang, F. Blaabjerg, and T. Kerekes, "A Hybrid Power Control Concept for PV Inverters With Reduced Thermal Loading," *IEEE Trans. Power Electron.*, vol. 29, no. 12, pp. 6271–6275, Dec. 2014.

[34] U. Bussemas, B. Burger, H. Schmidt, and S. Elies, "How Fast Does an MPP Tracker Really Need To Be?" in *Proc. 24th European Photovoltaic Solar Energy Conference*, Hamburg, Germany, Sep. 2009, pp. 3273–3276.

[35] E. Koutroulis and F. Blaabjerg, "A New Technique for Tracking the Global Maximum Power Point of PV Arrays Operating Under Partial-Shading Conditions," *IEEE J. Photovolt.*, vol. 2, no. 2, pp. 184–190, Apr. 2012.

[36] A. Kumaresan, H. D. Tafti, K. N. Kumar, G. G. Farivar, J. Pou, and T. Subbaiyan, "Flexible Power Point Tracking for Solar Photovoltaic Systems using Secant Method," *IEEE Trans. Power Electron.*, 2021, early access, doi: 10.1109/TPEL.2021.3049275.

[37] J. Fang, R. Zhang, H. Li, and Y. Tang, "Frequency Derivative-Based Inertia Enhancement by Grid-Connected Power Converters With a Frequency-Locked-Loop," *IEEE Trans. Smart Grid*, vol. 10, no. 5, pp. 4918–4927, Sep. 2019.

[38] C. Broderick, "Rate of Change of Frequency (RoCoF) withstand capability," ENTSOE, Brussels, Belgium, Tech. Rep., Jan. 2018.

Qiao Peng (S'18-M'21) received the B.Eng. degree in electrical engineering from Sichuan University, Chengdu, China, in 2015, and the Ph.D. degree from the Department of Energy Technology, Aalborg University, Denmark, in 2020.

She is currently an Assistant Research Fellow with the College of Electrical Engineering, Sichuan University, Chengdu, China. Her research interests include stability and control of power electronics-based power systems and grid-integration of renewable energy sources, especially photovoltaic systems.

Zhongting Tang was born in Sichuan, China, in 1990. She received her B.S. degree in Automation Control in 2012 and Ph.D. degree in Control Science and Engineering in 2020 from Central South University, Changsha, China. During 2018-2020, she studied as a guest Ph.D. student at the Department of Energy Technology in Aalborg University, Aalborg, Denmark, where she is currently working as a postdoc here.

Her research focus is on the grid integration of photovoltaics, topology and modulation technology of transformerless converter and its application and reliability in Photovoltaic system.

Yongheng Yang (SM'17) received the B.Eng. degree from Northwestern Polytechnical University, China, in 2009 and the Ph.D. degree from Aalborg University, Denmark, in 2014. He was a postgraduate student with Southeast University, China, from 2009 to 2011. In 2013, he spent three months as a Visiting Scholar at Texas A&M University, USA. Since 2014, he has been with the Department of Energy Technology, Aalborg University, where he became a tenured Associate Professor in 2018. In January 2021, he joined Zhejiang University, China, where he is now a ZJU100 Professor at the Institute of Power Electronics, College of Electrical Engineering.

Dr. Yang was the Chair of the IEEE Denmark Section (2019-2020). He is an Associate Editor for several IEEE Transactions/Journals. He is a Deputy Editor of the *IET Renewable Power Generation* for Solar Photovoltaic Systems. He was the recipient of the 2018 *IET Renewable Power Generation* Premium Award and was an Outstanding Reviewer for the IEEE TRANSACTIONS ON POWER ELECTRONICS in 2018. In addition, he has received two IEEE Best Paper Awards. Currently, he is the Secretary of the IEEE Power Electronics Society Technical Committee on Sustainable Energy Systems. His research includes the grid-integration of photovoltaic systems and control of power converters, in particular, the mechanism and control of grid-forming power converters and systems.

Tianqi Liu (SM'16) received the B.S. and the M.S. degrees from Sichuan University, Chengdu, China, in 1982 and 1986, respectively, and the Ph.D. degree from Chongqing University, Chongqing, China, in 1996, all in Electrical Engineering.

Currently, she is a professor in the College of Electrical Engineering, Sichuan University, Chengdu, China. Her main research interests are power system analysis and stability control, HVDC, optimal operation, dynamic security analysis and load forecast.

Frede Blaabjerg (S'86-M'88-SM'97-F'03) was with ABB-Scandia, Randers, Denmark, from 1987 to 1988. From 1988 to 1992, he got the PhD degree in Electrical Engineering at Aalborg University in 1995. He became an Assistant Professor in 1992, an Associate Professor in 1996, and a Full Professor of power electronics and drives in 1998. From 2017 he became a Villum Investigator. He is honoris causa at University Politehnica Timisoara (UPT), Romania and Tallinn Technical University (TTU) in Estonia.

His current research interests include power electronics and its applications such as in wind turbines, PV systems, reliability, harmonics and adjustable speed drives. He has published more than 600 journal papers in the fields of power electronics and its applications. He is the co-author of four monographs and editor of ten books in power electronics and its applications.

He has received 31 IEEE Prize Paper Awards, the IEEE PELS Distinguished Service Award in 2009, the EPE-PEMC Council Award in 2010, the IEEE William E. Newell Power Electronics Award 2014, the Villum Kann Rasmussen Research Award 2014 and the Global Energy Prize in 2019. He was the Editor-in-Chief of the IEEE TRANSACTIONS ON POWER ELECTRONICS from 2006 to 2012. He has been Distinguished Lecturer for the IEEE Power Electronics Society from 2005 to 2007 and for the IEEE Industry Applications Society from 2010 to 2011 as well as 2017 to 2018. In 2019-2020 he serves a President of IEEE Power Electronics Society. He is Vice-President of the Danish Academy of Technical Sciences too.